Future Energy
Open Access Journal
ISSN 2832-0328

February 2026| Volume 05 | Issue 01 | Pages 30-40
Journal homepage: https://fupubco.com/fuen
https://doi.org/10.55670/fpll.fuen.5.1.4

Future Publishing LLC

Article

Numerical study of MHD mixed convection in an oriented elliptic geometry under the influence of some selected geometrical variables and fluid flow properties saturated with Al_2O_3-water nanofluid

T. Adekeye[1]*, P.O. Okekunle[2], I. K. Adegun[3]

[1]Department of Mechanical Engineering, Faculty of Engineering and Technology, Kwara State University, Malete, Kwara State, Nigeria
[2]Department of Mechanical Engineering, Faculty of Engineering and Technology, Ladoke Akintola University of Technology, Ogbomoso, Oyo State, Nigeria
[3]Department of Mechanical Engineering, Faculty of Engineering and Technology, University of Ilorin, Ilorin, Kwara State, Nigeria

ARTICLE INFO

Article history:
Received 29 September 2025
Received in revised form
12 November 2025
Accepted 08 December 2025

Keywords:
Elliptic configuration, Al_3O_2-water nanofluid, MHD Fluid flow, Heat transfer, Velocity profiles, Temperature field

*Corresponding author
Email address:
tundeadekeye2008@gmail.com

DOI: 10.55670/fpll.fuen.5.1.4

ABSTRACT

This study numerically investigated the effects of some selected geometrical parameters, such as inclination angles, eccentricity, and some fluid flow properties, such as nanoparticle volume fractions, Grashof, Hartmann, Reynolds, Prandtl, and Richardson numbers, on fluid flow pattern (velocity profiles), temperature history, and heat transfer rate in an inclined elliptic configuration filled with Al_2O_3-H_2O nanofluid. The non-dimensional governing equations were developed for the elliptic geometry. The lower wall of the configuration was subjected to continual heat flux, and the top wall was retained at a persistent cold temperature (T_c) while the cross-sectional ends of the configuration were presumed to be insulated. The normalized controlling equations were explained using a 4th order Alternating Direction Implicit (ADI) scheme with the Gauss-Seidel iteration technique. A computer code was written with Python 3.X version to simulate the fluid flow and heat transfer in the enclosure. The numerical results obtained exhibited that fluid flow circulation deteriorated with increasing Hartmann number and increasing nanoparticle volume fraction individually. The rate of heat transfer (Nu) augmented with fluid flow circulation for the range of Grashof at 10^4-10^6 and $\varphi=0.0$-0.045, respectively. The temperature field decreased with increasing nanoparticle volume fractions (0.00, 0.025, and 0.045). It was revealed from the outcomes that the optimum heat transfer rates were attained in the configuration for eccentricity, e value at 0.866, and inclination angle in the range $0^\circ < \theta < 60^\circ$, correspondingly. The average rate of heat transfer is elevated with increasing Reynolds number under laminar conditions. The results obtained could be applied in metallurgical industries where a magnetic field is used to regulate the flow of hot fluid. It could also be useful in the development of a model for designing a compact MHD heat exchanger for industrial applications.

1. Introduction

In the last decades, energy matters have been a serious concern among other choices, strategies, and policies for human survival and development. It is compulsory for most production processes and other economic activities, and it is an integral component of Oyedepo's way of life [1]. However, finding appropriate energy conversion techniques, geometries, and working fluids for satisfactory and reliable performance, as well as achieving heat transfer augmentation at reduced operational cost, has been a serious concern across various systems. In the same vein, the cooling efficiency required for micro-electronic equipment, transportation systems, and manufacturing processes requires the combination of a base fluid (water) and a nanoparticle for optimal performance and efficiency, as reported by Ruchika et al. [2]. Mixed convective heat transfer and fluid flow in irregularly shaped geometry are significant in engineering and technology because of their numerous applications, such as cooling of microelectronic equipment, heat exchangers, and solar collectors Al-salem et al. [3]. Free and forced convective flows, as well as heat transfer in enclosures, have been extensively examined due to their numerous engineering applications, such as ventilation of rooms, lubrication technologies, nuclear reactors, drying technologies, food processing, solar-powered systems, and others [4-5]. According to Morley et al. [6], any movement of an electrically conducting material in a magnetic field that generates electric current, which in turn induces its own magnetic field, is called magnetohydrodynamic (MHD). Examples of such are liquid metals, plasma, electrolyte, or ionized gas, and nanofluids. It has numerous industrial applications, originally in astrophysics, as in solar structure and geophysics, as in planetary magnetism, MHD pumps, MHD generators, nuclear reactors, electromagnetic casting, metallurgical processing, stability of convective flows, and several others [7-9].

The analysis of magnetohydrodynamics (MHD) flow and heat transfer is often experienced in electrical power generation, solar structures, and magnetism [10]. Also, further engineering and industrial circumstances where mixed convective flow in the presence of a magnetic field is relevant include cooling of electronic devices, furnace design flow, and heat transfer in obstructed cavities such as micro-electronic devices, flat plate condensers in refrigeration systems, production of steel and aluminum, high-performance super-alloys, or crystal, among others [10-11]. Wisam and Gregory [12] reported MHD flow in a cylindrical-circular configuration. The result indicated that the heat transfer enhancement was 58 %. Fatih and Hakan [13] presented MHD mixed convection in a nanofluid saturated lid-driven square-cylinder cavity. They concluded that heat transfer improvement moved towards both ends of the lower wall but decreased within the parametric range of less than $0.5 \leq x \leq 1$. Alam and Kham [14] reported MHD effects on mixed convection flow through an open diverging channel-circular impediment. The results indicated that the rate of heat transfer and the fluid's mean temperature changed rapidly with the Richardson number (Ri), but increased with increasing Reynolds (Re), Prandtl (Pr), and Hartmann number (Ha). Muhammad et al. [15] analyzed MHD natural convection in a trapezoidal cavity with a circular block. They concluded that the local Nusselt number has an optimum value near the wall edge, but the opposite was true near the wall midpoint, despite the bottom wall being subjected to the same condition. Sourtiji et al. [16] studied MHD natural convection heat transfer in a cylindrical-triangular combination. The results indicated that fluid flow was inhibited by the retarding force, and the magnetic field effect increased as the Nusselt number decreased.

Mahfoud [17] reported heat transfer in a cylinder under the influence of a magnetic field. The result showed that high values of the Richardson number led to low Reynolds numbers in critical condition. Sharma and Konwar [18] studied MHD flow in a porous medial cylindrical geometry. The results showed that the Soret, Dufour, and Grashof numbers have a significant effect on flow velocity, while the Reynold, Hartmann, and Lewis numbers have little impact on the velocity profiles. Moreover, it is important to note that the excellent performance of any electronic equipment is predicted by its operating temperature. Continuous cooling is highly needed to keep electronic devices within the expected temperature range. Increasing heat transfer rate, compactness, and reliable operation are the problems confronting electronic device experts and researchers. These problems have drawn the attention of investigators and Engineers to intensify their efforts on studying mixed convective heat transfer since it is the source of the air-cooling system used [19-20]. Nanofluids, on the other hand, are dilute liquid suspensions of nanoparticles or mixtures of a base fluid with a very small amount of solid metallic oxides with at least one critical dimension smaller than 100 nm, as first used by Choi [21].

In recent years, more attention has been paid to nanotechnology due to its enhanced heat-transfer properties. Nanofluid is useful in buildings, heating, heat exchangers, power plants, automobile cooling applications, cooling of electronic devices, cooling of transformer coils, the transportation industry, microchips, and solar absorption, to mention a few. The roles of nanofluids are numerous, considering the heat exchanger devices for different engineering and industrial applications [21]. Adekeye et al. [22] investigated MHD in an inclined elliptic porous medium with uniform heat flux. They concluded that maximum heat transfer was achieved at eccentricity, e value of 0.8. Also, heat transfer enhancement was significant within the parametric range $58° \leq \theta \leq 90°$. Chamkha et al. [23] studied the impact of a moving cone on the mixed convection in a double lid-driven 3D porous trapezoidal nanofluid-filled cavity under the influence of a magnetic field. The finite element technique was employed. The results showed that heat transfer augmentation is achieved with CNT particles at a reduced magnetic field strength. Also, the result revealed that the cone's aspect ratio can augment heat transfer by up to 95%. Armaghani et al. [24] investigated MHD mixed convection of nanofluid in an open C-shaped enclosure. The results showed that increasing the Hartmann number enhanced heat transfer. Also, a high Reynolds number led to enhanced heat transfer, while an increased nanofluid volume fraction improved it further. Shukla et al. [25] investigated MHD mixed convection nanofluid multiple-slip flow and heat transfer in a vertical cylinder, considering entropy generation. The homotopy analysis method (HAM) was employed. They concluded that there is an increase in temperature due to an increase in curvature and the applied magnetic field, but this effect decreases with the Richardson number. Tayebi and Chamkha [26] investigated MHD natural convection heat transfer of a hybrid Al_2O_3 Cu/water nanofluid in a square enclosure in the presence of a wavy-circular conductive cylinder. The researchers concluded that the strength of flow circulation significantly increased with increasing Rayleigh number and decreasing Hartmann number.

Based on the reviewed literature, research is extremely limited in elliptic geometry, especially for MHD systems using nanofluid as the working fluid. Also, to the best of the researchers' knowledge, no article has considered investigating MHD mixed convection nanofluid flow in an oriented elliptic enclosure under a continuous heat flux boundary condition. This identified gap motivated the writers to investigate MHD mixed convective fluid flow in an oriented elliptic configuration with constant heat flux and a Prandtl number of 6.2, which targeted at improving a more compact, effective, efficient, and durable heat exchanger for industrial applications (Adegun et al. [27]).

2. Methodology

2.1 Description of the problem of elliptic geometry

The physical illustration of the problem is presented in Figure 1. The upper partition was air-cooled and kept at a constant temperature (T_c). The lower wall of the geometry was heated and maintained at a constant temperature (T_h) while the cross-sectional ends of the configuration were assumed to be adiabatic. The cavity was saturated with Al_2O_3-water nanofluid, which is electrically conducting and under the control of a magnetic field (B_0), which was applied in radial direction on the elliptic-cylindrical wall of the configuration at an inclined angle θ. The Grashof number (Gr) was considered to be $10^4 \leq Gr \leq 10^6$. The Hartmann number was within the range $0 \leq Ha \leq 100$ at an interval of 10 while the Prandtl number was assumed to be constant at Pr = 6.2. Eccentricity was varied between 0 and 0.9 at an interval of 0.1, and the elliptic inclination angle was employed as $0° \leq \theta \leq 90°$ at an interval of 30°. The Reynolds number (Re) was varied from 100 to 1900 in increments of 100, while nanoparticle concentrations ranged from 0.00 to 0.045.

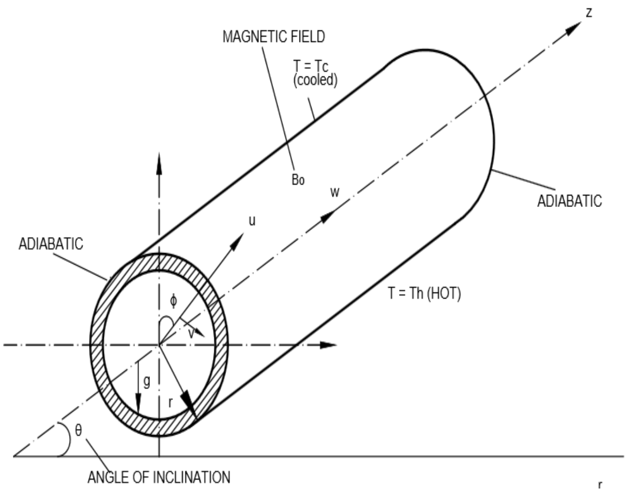

Figure 1. Physical Illustration with boundary conditions

2.2 Basic assumptions

The following model conventions were considered in this study:

- The fluid flow is considered to be 3-D (r,ϕ, z) laminar flow.
- Unsteady state situation is assumed, that is:

$$\frac{\partial U}{\partial t}=\frac{\partial V}{\partial t}=\frac{\partial W}{\partial t}=\frac{\partial T}{\partial t}\neq 0 \tag{1}$$

- Velocity constituents at the wall are zero

$$U_r = U_\phi = U_z = 0 \text{ (no slip boundary)} \tag{2}$$

- Radiation and Joule heating effects are ignored.
- The flow density is assumed constant.

2.3 Governing equations

The principal equations for incompressible flow from the Stokes equation in polar or cylindrical coordinates were presented, including nanofluid parameters and modifications (Bird et al., [28]). The continuity equation, in a dimensional form, the conservation of energy was given as:

$$\frac{1}{r}.\partial\left(r.\frac{U_r}{\partial r}\right)+\frac{1}{r}.\partial\left(\frac{U_\phi}{\partial\phi}\right)+\frac{\partial Uz}{\partial Z}=0 \tag{3}$$

The dimensional momentum equations are in radial (r), azimuthal (Φ) and axial (z) directions from the modified existing equation (Navier-Stokes) for polar coordinates were given as follows:

For r-component (radial direction): The primitive form of the governing equation for momentum in radial (r) is given as:

$$\rho\left(\frac{\partial U_r}{\partial t}+U_r.\frac{\partial U_r}{\partial r}+\frac{U_\phi}{r}.\frac{\partial U_r}{\partial\phi}-\frac{U_{\phi^2}}{r}+U_z.\frac{\partial U_r}{\partial z}\right)=-\frac{1}{\rho_{nf}}.\frac{\partial P}{\partial r} + \rho g\beta_{nf}(t-t_{ref})Cos\theta+\upsilon_{nf}\left[\frac{\partial^2 U_r}{\partial r^2}+\frac{\partial U_r}{r\partial r}-\frac{U_r}{r^2}+\frac{1}{r^2}.\frac{\partial^2 U_r}{\partial\phi^2}-\frac{2}{r^2}.\frac{\partial U_\phi}{\partial\phi}+\frac{\partial^2 U_r}{\partial Z^2}\right]-\frac{\sigma_{nf}{B_0}^2\upsilon}{\rho_{nf}} \tag{4}$$

Φ-component (azimuthal direction): The momentum equations in azimuthal (Φ) direction is given as:

$$\rho\left(\frac{\partial U_\phi}{\partial t}+U_r.\frac{\partial U_\phi}{\partial r}+\frac{U_\phi}{r}.\frac{\partial U_\phi}{\partial\phi}+\frac{U_r U_\phi}{r}+U_z.\frac{\partial U_\phi}{\partial z}\right)=-\frac{1}{\rho_{nf}}-\frac{1}{r}.\frac{\partial P}{\partial\phi}+g\beta_{nf}(t-t_{ref})Sin\theta+\left[\frac{\partial^2 U\phi}{\partial r^2}+\frac{\partial U\phi}{r\partial r}-\frac{U\phi}{r^2}+\frac{1}{r^2}.\frac{\partial^2 U\phi}{\partial\phi^2}+\frac{2}{r^2}.\frac{\partial Ur}{\partial\phi}+\frac{\partial^2 U\phi}{\partial Z^2}\right]-\frac{\sigma_{nf}{B_0}^2\upsilon}{\rho_{nf}} \tag{5}$$

Z-component (axial direction): The momentum equations in axial (z) direction is given as:

$$\rho\left(\frac{\partial U_z}{\partial t}+U_r.\frac{\partial U_z}{\partial r}+\frac{U_\phi}{r}.\frac{\partial U_z}{\partial\phi}+U_z.\frac{\partial U_z}{\partial z}\right)=-\frac{\partial P}{\partial z}+g\beta_{nf}(t-t_{ref})+\upsilon_{nf}\left[\frac{\partial^2 U_z}{\partial r^2}+\frac{\partial U_z}{r\partial r}+\frac{1}{r^2}.\frac{\partial^2 U_z}{\partial\phi^2}+\frac{\partial^2 U_z}{\partial Z^2}\right]-\frac{\sigma_{nf}{B_0}^2\upsilon}{\rho_{nf}} \tag{6}$$

Energy equation: The energy equation is computed as:

$$\frac{\partial T}{\partial t}+u_r\frac{\partial T}{\partial v}+\frac{u_\phi}{v}\ .\ \frac{\partial T}{\partial\phi}+u_z\frac{\partial T}{\partial z}=\frac{q_g}{C_p}+\alpha\left[\frac{\partial^2 T}{\partial v^2}+\frac{1}{v^2}.\frac{\partial^2 T}{\partial\phi^2}+\frac{\partial^2 T}{\partial z^2}\right]+\frac{S+H}{K} \tag{7}$$

Where

$$S=2\mu\left[\left(\frac{\partial u_r}{\partial}\right)^2+\left(\frac{1}{v}.\frac{\partial u_\phi}{\partial\phi}+\frac{u_r}{v}\right)^2+\left(\frac{\partial u_z}{\partial z}\right)^2\right] \tag{8}$$

$$H=\mu\begin{bmatrix}\left(\frac{1}{v}.\frac{\partial u_r}{\partial\phi}+\frac{\partial u_\phi}{\partial v}-\frac{u_\phi}{v}\right)^2+\\ \left(\frac{\partial u_\phi}{\partial z}+\frac{1}{v}.\frac{\partial u_z}{\partial\phi}\right)^2+\left(\frac{\partial u_z}{\partial v}+\frac{\partial u_r}{\partial z}\right)^2\end{bmatrix} \tag{9}$$

$$K=\rho c_p \tag{10}$$

2.4 Normalized variables

The quantities in this section are employed to develop the non-dimensionalized governing equations and boundary conditions.

$$R=\frac{r}{d},\ U=\frac{U_r d}{\upsilon},\ V=\frac{U_\phi d}{\upsilon},W=\frac{U_z d}{\upsilon},$$

$$z=Zd,P=\frac{p}{p_{ref}},\ T=\frac{t-t_{ref}}{\Delta t},$$

$$\Delta T=\frac{qd}{k},\ Pr=\frac{\upsilon}{\alpha}=\frac{\rho C_p\upsilon}{k},\ Ra=\frac{g\beta\Delta T d^3}{\upsilon\alpha},$$

$$Ha=\frac{\sigma_{nf}{B_0}^2 d^3}{\rho^2{}_{nf}\upsilon},\text{modified Re}=\frac{V_{nf}d^3}{\rho_{nf}\upsilon^2},\text{Gr}=\frac{\beta_{nf}g\Delta T d^3}{\nu^2},$$

$$\text{Ri}=\frac{Gr}{Re^2}\text{ or }\frac{Ra}{Pr.Re^2},U_R=\frac{1}{R}\frac{\partial\psi}{\partial\phi},\ U_\phi=-\frac{\partial\psi}{\partial R},$$

$$D_h=\frac{4A}{P}$$

2.5 Model interface conditions

The border conditions used in this study are:
The borderline condition along the walls of the elliptic duct was

(a) There was no slip boundary, that is:

$$U_r = U_{\phi} = U_z = 0 \tag{11}$$

(b) There was no temperature gradient, that is,

$$\frac{\partial T}{\partial r} = 0 \tag{12}$$

The upper elliptic wall surface was kept at constant cold temperature *(Tc),* and it was expressed as:

$$U_r = U_{\phi} = U_z = \mathrm{T} = 0 \tag{13}$$

The lower elliptic wall surface of the configuration was subjected to a constant heat flux, and it was expressed as

$$\frac{\partial q}{\partial r} = 0 \tag{14}$$

The radial temperature gradient of the two cross-sectional ends of elliptic geometry was considered adiabatic, expressed as:

$$\frac{\partial T}{\partial r} = 0 \tag{15}$$

2.6 Normalized governing equations

The normalized governing equations obtained using the normalization variables are given as:
From equations (1) and by applying the normalized variable, we have,

$$\frac{\partial U}{\partial R} + \frac{U}{R} + \frac{1}{R}.\frac{\partial V}{\partial \phi} + \frac{\partial W}{\partial Z} = 0 \tag{16}$$

From Eq (4), taken ρ = constant and employing the normalized variables is expressed as:

$$\frac{\partial U}{\Delta t} + U.\frac{\partial U}{\partial R} + \frac{V}{R}.\frac{\partial U}{\partial \phi} - \frac{V^2}{R} + W.\frac{\partial U}{\partial Z} = -\left(\frac{1}{{\rho^2}_{nf}}.\frac{\partial P}{\partial R}\right) + Gr_{nf} Cos\theta + Re_{nf}\left[\frac{\partial^2 U}{\partial R^2} + \frac{1}{R}.\frac{\partial U}{\partial R} - \frac{U}{R^2} + \frac{1}{R^2}.\frac{\partial^2 U}{\partial \phi^2} - \frac{2}{R^2}.\frac{\partial V}{\partial \phi} + \frac{\partial^2 U}{\partial z^2}\right] - {Ha^2}_{nf} \tag{17}$$

From Eq (5), taken ρ= constant, and applying the normalized variables gives:

$$\frac{\partial V}{\Delta t} + U.\frac{\partial V}{\partial R} + \frac{V}{R}.\frac{\partial V}{\partial \phi} + U.\frac{V}{R} + W.\frac{\partial V}{\partial Z} = \left(-\frac{1}{{\rho^2}_{nf}}.\frac{1}{R}.\frac{\partial P}{\partial \phi}\right) + Gr_{nf} Sin\theta + Re_{nf}\left[\frac{\partial^2 V}{\partial R^2} + \frac{1}{R}.\frac{\partial V}{\partial R} - \frac{V}{R} + \frac{1}{R^2}.\frac{\partial^2 V}{\partial \phi^2} + \frac{2}{R^2}.\frac{\partial U}{\partial \phi} + \frac{\partial^2 V}{\partial z^2}\right] - {Ha^2}_{nf} \tag{18}$$

From Eq (4), taken ρ= constant, and applying the normalized variables gives:

$$\frac{\partial W}{\Delta t} + U.\frac{\partial W}{\partial R} + \frac{V}{R}.\frac{\partial W}{\partial \phi} + W.\frac{\partial W}{\partial Z} = \left(-\frac{1}{\rho_{nf}}.\frac{\partial P}{\partial z}\right) + Gr_{nf} Sin\theta + Re_{nf}\left[\frac{\partial^2 W}{\partial R^2} + \frac{1}{R}.\frac{\partial W}{\partial R} + \frac{1}{R^2}.\frac{\partial^2 W}{\partial \phi^2} + \frac{\partial^2 W}{\partial z^2}\right] - {Ha^2}_{nf} \tag{19}$$

From Eq(5), keeping k constant and applying the normalized variables is expressed as:

$$\frac{\partial \mathrm{T}}{\Delta \mathrm{T}} + \left[U.\frac{\partial \mathrm{T}}{\partial \mathrm{R}} + \frac{\mathrm{V}}{R}.\frac{\partial \mathrm{T}}{\partial \phi} + W.\frac{\partial \mathrm{T}}{\partial \mathrm{z}}\right] = \mathrm{T} + Pr_{nf}\left[\left(\frac{\partial^2 \mathrm{T}}{\partial \mathrm{R}^2} + \frac{1}{\mathrm{R}^2}.\frac{\partial^2 \mathrm{T}}{\partial \phi^2} + \frac{\partial^2 \mathrm{T}}{\partial \mathrm{z}^2}\right)\right] + 2\alpha_{nf}\left[\frac{\partial^2 \mathrm{U}}{\partial \mathrm{R}^2} + \frac{\partial^2 \mathrm{V}}{\partial \phi^2} + \frac{U^2}{\mathrm{R}^2} + \frac{\partial^2 \mathrm{W}}{\partial \mathrm{Z}^2}\right] + \alpha_{nf}\left[\frac{\partial^2 \mathrm{U}}{\partial \phi^2} + \frac{\partial^2 \mathrm{V}}{\partial \mathrm{R}^2} - \frac{V^2}{\mathrm{R}^2} + \frac{\partial^2 \mathrm{V}}{\partial \mathrm{Z}^2} + \frac{1}{\mathrm{R}^2}.\frac{\partial^2 \mathrm{W}}{\partial \phi^2} + \frac{\partial^2 \mathrm{U}}{\partial \mathrm{R}^2} + \frac{\partial^2 \mathrm{U}}{\partial \mathrm{Z}^2}\right] \tag{20}$$

2.7 Thermo-physical properties of nanofluid

Several studies (numerical and experimental) have estimated the nanoparticle properties based on the base fluid and the nanoparticle. The conventional model obtained for a two-phase mixture with numerous experimental results is presented by researchers (Wang et al. [29]). For this study, the under-listed equations were adopted for the thermo-physical properties.

$$\rho_{nf} = (1 - \varphi)(\rho_{bf} + \varphi\rho_p) \tag{21}$$

The product of the density and specific heat capacity of the nanofluid was estimated according to Equation 22.

$$(\rho C_p)_{nf} = (1 - \varphi)\,(\rho C_p)_{bf} + \varphi(\rho C_p)_p \tag{22}$$

The thermal expansion coefficient of the nanofluid was estimated by Equation 23.

$$(\rho_\beta)_{nf} = (1 - \varphi)(\rho_\beta)_{bf} + \varphi(\rho_\beta)_p \tag{23}$$

The dynamic viscosity of the nanofluid was calculated according to Equation 24.

$$\mu_{nf} = \mu_{bf}(123\varphi^2 - 7.3\varphi + 1 \tag{24}$$

The thermal conductivity of the nanofluid was calculated according to Equation 25.

$$\frac{K_{nf}}{K_{bf}} = \left[\frac{K_p + 2K_{bf} - 7.3\varphi(K_{bf} - K_p)}{K_p + 2K_{bf} - \varphi(K_{bf} - K_p)}\right] \tag{25}$$

The thermal diffusivity of the nanofluid was estimated according to Equation 26.

$$\alpha_{nf} = \frac{K_{nf}}{(\rho_{C_p})_{nf}} \tag{26}$$

The electrical conductivity of the nanofluid was calculated according to Equation 27.

$$\sigma_{nf} = (1 - \varphi)\sigma_{bf} + \varphi_p \tag{27}$$

Where bf – basefluid, nf – nanofluid, P – solid particles [30].

2.8 Solution technique and computational procedure

The non-dimensional major equations with their thermal periphery conditions were explained numerically by applying the Gauss-Seidel technique. For the discretization of the governing equations, 4th order Alternating Direction Implicit (ADI) scheme was employed. Algebraic equations achieved for each variable were solved by a simple form of the Gauss-Seidel iterative technique. Merging criteria, (10^{-6}) was selected for all dependent variables, and the value of (0.1) was used for the under-relaxation (Adegun et al. [27]). Subsequently, the rate of heat transfer (NU), the heat transfer coefficient, was realized when the criterion was satisfied.

Half of the cross-section for laminar mixed convection flow in an elliptic configuration saturated with Al_2O_3-water nanofluid was used in the numerical computation. The velocity summaries were numerically determined from the momentum transport equation and its associated boundary conditions. The velocity derived was then used to determine the energy transport equation for the generation of the temperature history of the fluid region. Computed values for Nusselt number, mean axial velocity, fluid temperature distribution, effect of eccentricity on the enclosure, and rate of heat transfer in the configuration were determined from different dimensionless controlling parameters, Grashof, Hartmann, Reynolds, Richardson number, and enclosure inclination angle.

To create the grid independence of the solution scheme, grid-function convergence assessments were carried out on four non-uniform grid mesh sizes as shown in Table 1. Different grid sizes were considered for the conditions at θ = 30^0, Gr = 10^6, Pr = 6.2, Ha = 50, Re=300, e = 0.866, ϖ = 0.025. The grid sizes were determined after a quantity of initial runs, and the impact on numerical results was investigated. The code was examined for grid independence by calculating the average Nusselt number along the lower heated wall of the geometry. Grid mesh sizes for the radial, azimuthal, and axial directions were 30, 56, and 50, respectively. The convergence criterion employed for the termination of all computation was $\max_{grid}|r^{n+1}-r^n|\leq\varepsilon$ where n is the iteration number and r represents the self-determining variables (U, V, W, T) and $\varepsilon=10^{-6}$ [31]. Simulation converged when the percentage error was less than or equal to 0.001. Also, for the validation of the present numerical results to establish the accuracy of the mathematical model, the present results on average Nusselt number were compared with reported studies by Javey [32], Sakalis et al. [33], and Adegun et al. [27] as presented in Table 2.

2.9 Heat Transfer Analysis

For accurate determination of temperature values, convective heat transfer coefficient, h (z), from Newton's law of cooling, expressed as,

$$h\,(z)\ = \frac{q''net}{T_w(z)-T_f(z)} \tag{28}$$

Where $q''net$ is the net heat flux, T_w and T_f are the wall and fluid temperatures, respectively, while z was taken as the axial distance in the test section between the inlet and outlet, also, from the relation.

$$q = q_{conv} = q_{cond} \tag{29}$$

Table 1. Assessment of the average Nusselt number at the lower heated hedge of the elliptic configuration for diverse grid determination at θ = 30^0, Gr = 10^6, Pr = 6.2, Ha = 50, Re=300, e = 0.866, ϖ = 0.025

Mesh sizes	10 × 36 ×30	20 × 46 × 40	30 ×56 × 50	40 × 66 × 60
Nu_{av}	4.736	4.759	4.768	4.774
% error	0.005280	0.003051	0.001093	0.0

Table 2. Evaluation of average Nusselt numbers at Pr=0.71, Ha=φ=0, Aspect ratio (AR)=0.25

S/N	Present study	Published results	Deviation (%)
1	4.782	4.891 (Javery [32])	2.28
2	4.782	4.711 (Sakalis et al. [33])	1.48
3	4.782	4.792 (Adegun et al. [27])	0.21

Expressing Equation 29 gave

$$q = h\,(T_w - T_f) = k\frac{\partial T}{\partial r} \tag{30}$$

$$h\,(z) = \frac{Kf\frac{\partial T}{\partial r}}{Tw-Tf} \tag{31}$$

Where T_w = temperature of the wall, T_f = temperature of the fluid, $\frac{\partial T}{\partial r}$= temperature gradient.

For the corresponding local axial rate of heat transfer (Nusselt number), the mathematical expression was given as,

$$NU_L = \frac{h(z).D_h}{K_f} \tag{32}$$

Where NU_L = Local Nusselt number, h(z) = convective heat transfer coefficient in axial direction, K_f = thermal conductivity of the fluid, D_h = hydraulic diameter.

But the hydraulic diameter (D_h) was defined as:

$$D_h = \frac{4A_c}{P_w} \tag{33}$$

Where A_c = πab (cross-sectional area), P_w = π(a+b) wetted perimeter:

$$D_h = \frac{4A_c}{P_w} = D_h = \frac{4(\pi ab)}{\pi(a+b)} = \frac{4\pi(ab)}{\pi(a+b)} \tag{34}$$

Further simplification gave

$$\frac{4ab}{(a+b)}$$

$$\frac{4x1x\sqrt{1-e^2}}{1+\sqrt{1-e^2}}$$

$$\frac{4\sqrt{1-e^2}}{1+\sqrt{1-e^2}} \tag{35}$$

Substituting Equations 31 and 35 into Equation 32 gives:

$$NU_L = \frac{\frac{Kf\frac{\partial T}{\partial r}}{Tw-Tf}.4\sqrt{1-e^2}}{Kf.1+\sqrt{1-e^2}}$$

$$NU_L = \frac{\frac{\frac{\partial T}{\partial r}}{Tw-Tf}.4\sqrt{1-e^2}}{1+\sqrt{1-e^2}} \tag{36}$$

Where e is the eccentricity of an ellipse.

The average Nusselt number is defined as;

$$Nu_a = \frac{1}{\pi r}\int_0^{\pi} Nu(\phi)d\phi \tag{37}$$

For a uniform heat flux boundary conditions, the fluid temperature axial profile in the test section deduced from the energy balance equation was defined as:

$$T_f(z)\ = T_{entrance} + \frac{q''net\pi DL}{mC_p}z \tag{38}$$

Where $T_{entrance}$, m and C_p represent the fluid temperature at the entrance of the test section, the mass flow rate and fluid heat capacity respectively (Amino [34], Mansour et al. [35], Adekeye et al. [21]).

3. Results and Discussions

Figure 2 presents numerical results with the one published by Selimenfegidil and Oztop[30] for a cylindrical cavity for variation of Grashof number against average Nusselt number. The result was in very good agreement, with a 9% deviation across all conditions considered.

3.1 Velocity profiles

Figure 3 depicts the differences in mean axial velocity across various Hartmann numbers (Ha) and nanoparticle volume fractions. From the plot for Ha = 0, the fluid flow velocity increased by the buoyancy force (natural convection effect) prevailing in the configuration. On the other hand, for the Hartmann number (Ha) at 50 and 100, the Laplace force generated by the magnetic field effect became stronger than the buoyancy force and conversely reduced the fluid flow movement in the geometry (Ahmed et al. [8]) with different Reynolds numbers and varying nanoparticle volume fractions.

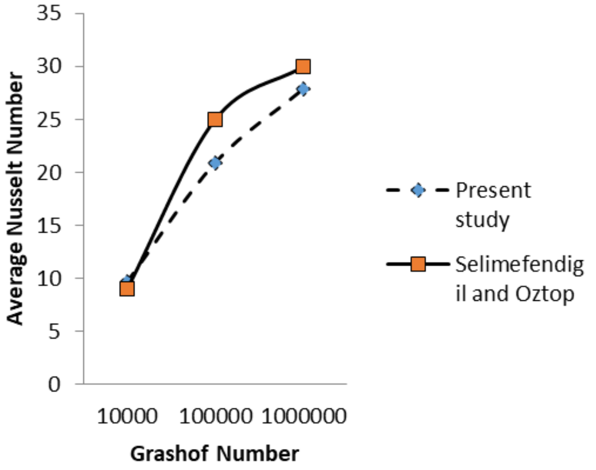

Figure 2. Relationship of present study for the case of $Gr = 10^4 – 10^6$, $\varphi = 2\%$ with Selimefendigil and Oztop [28]

It was indicated that the axial velocity increased gradually with Reynolds number. Also, it was observed that in the range $0 \leq Re \leq 100$, the fluid flow velocities were almost identical for other conditions considered. Above this range, $100 \leq Re \leq 1900$, the impact of Reynolds number and inclination angle became evident on the fluid flow strength. Figure 5 shows the variation of mean axial velocity with various values of eccentricities and nanoparticle volume fractions. It was revealed from the plot that the mean axial velocity augmented monotonically with the eccentricity but decreased with the elevating nanoparticle volume fractions due to insignificant convection impact within the range $0 \leq e \leq 0.4$. But the fluid circulation became pronounced, steady, and rigorous above this limit, that is, $0.7 \leq e \leq 0.866$ due to convection that became stronger than the heat transfer process. Figure 6 shows the variation of mean axial velocity with different inclination angles and varying nanoparticle volume fractions. From the Figure, it was discovered that fluid flow motion was significant within the range $0^0 \leq \theta \leq 60^0$. But above 60° , that is, ($60^0 \leq \theta \leq 90°$), the impact of inclination became insignificant owing to the gravitational force not having a noteworthy impact on the fluid flow again [27]. Figure 7 represents the variation of mean axial velocity with different Grashof numbers and nanoparticle volume fractions. From the Figure, it was shown that when $Gr = 10^4$, the extent of the fluid flow was small as a result of the insignificant influence of the buoyancy force, but when the values of the Grashof number increased to 10^5 and 10^6, the fluid flow motion increased due to the buoyancy force [8].

3.2 Temperature history

Figure 8 displays the disparity of bulk fluid temperature with different Reynolds numbers and nanoparticle volume fractions. The Plot shows the significance of the Reynolds number on the bulk fluid temperature. For all conditions at Re=1500, a slight steep valley was observed, indicating a critical flow condition that led to velocity instability due to flow separation. Figure 9 presents the variation of bulk temperature with different Hartmann numbers and nanoparticle volume fractions. The Figure shows that the bulk fluid temperature decreased with increasing Hartmann number and nanoparticle volume fraction, due to frictional and Brownian effects. Figure 10 presents the distinction of bulk fluid temperature with different angles of inclination and nanoparticle volume fractions. It was observed from the Figure that a similar trend of temperature behavior elevating progressively with the inclination angle for the range $0^0 \leq \theta \leq 60^0$. Above this limit, no important change was seen. Figure 11 shows the discrepancy of the non-dimensional temperature profiles with different nanoparticle volume fractions. It was observed from the Figure that the cooling efficiencies exhibited by different nanoparticle volume fractions. φ=0.045 changed the wall temperature profile and, conversely, reduced it. At Z=600 mm, a slight steep valley was observed, for the same reason stated in Figure 8.

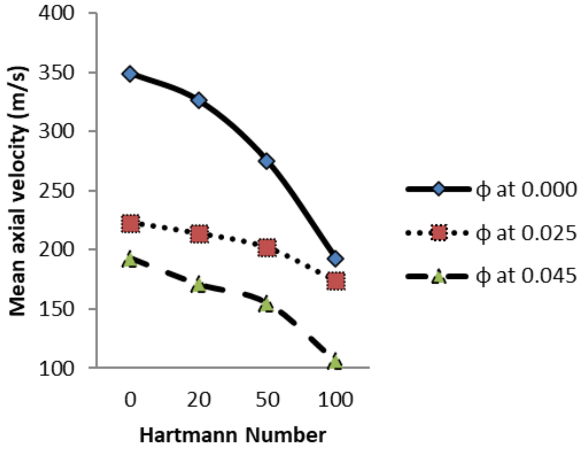

Figure 3. Variation of mean axial velocity with various values of Hartmann number at $\theta = 30^0$, $Gr = 10^6$, $Pr = 6.2$, $Re = 300$, $e = 0.866$, ω =0, 0.025, 0.045

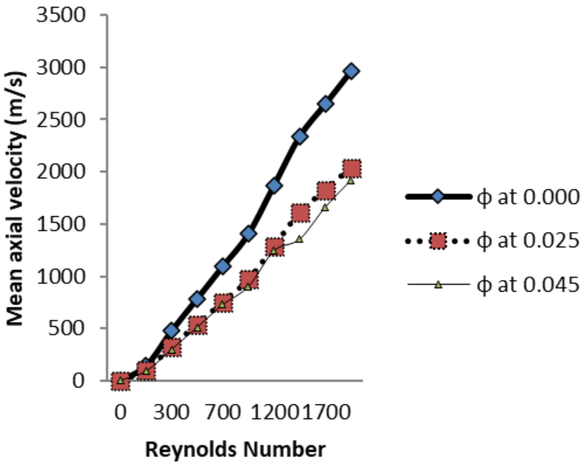

Figure 4. Distinction of mean axial velocity with different values of Reynolds number for a uniform heat flux at $\theta = 30^0$, $Gr = 10^6$, $Pr = 6.2$, $Re = 300$, $e = 0.866$, ω =0, 0.025, 0.045

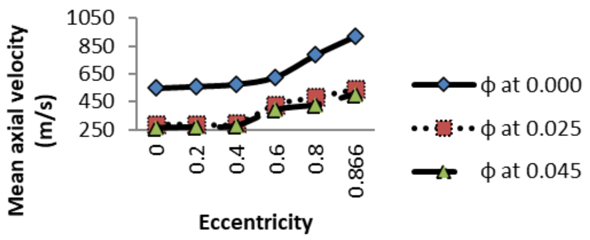

Figure 5. Variation of mean axial velocity with different values of eccentricities at θ = 30^0, Gr = 10^6, Pr = 6.2, Ha = 50, Re = 300 and ω =0, 0.025, 0.045

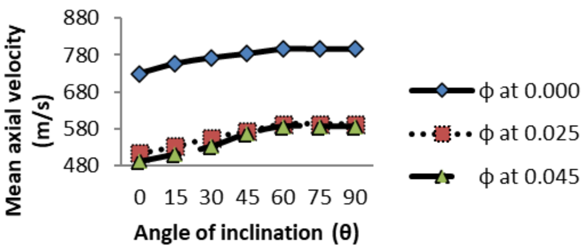

Figure 6. Deviation of mean axial velocity with different inclination angles at Gr = 10^6, Pr = 6.2, Re = 300, e = 0.866, Ha = 50, ω =0, 0.025, 0.045

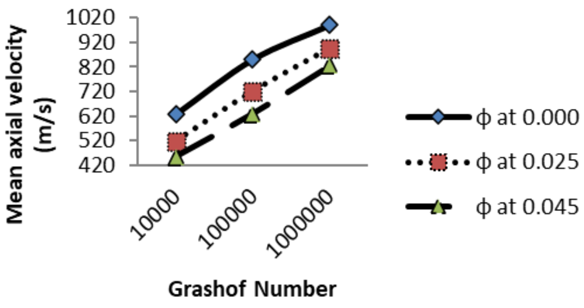

Figure 7. Variation of mean axial velocity with different Grashof number at θ = 30^0, Pr = 6.2, Re = 300, e = 0.866, Ha = 50 and ω = 0, 0.025 , 0.045

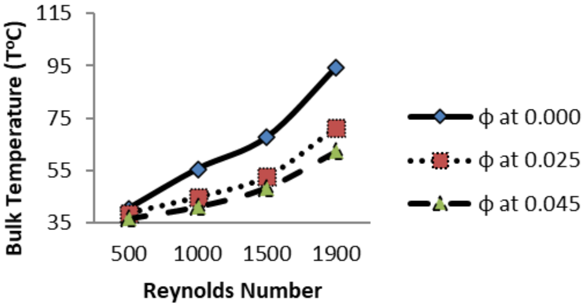

Figure 8. Variation of bulk temperatures with Reynold number at θ = 300, Gr = 106, Pr = 6.2, Ha = 50, e = 0.866, ω = 0, 0.025 , 0.045

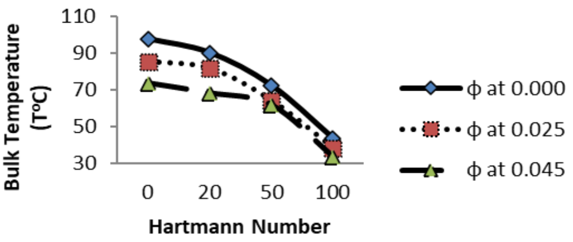

Figure 9. Variation of bulk temperatures with various Hartmann number at θ = 30^0, Gr = 10^6, Pr = 6.2, Re = 300, e = 0.866, ω = 0, 0.025, 0.045

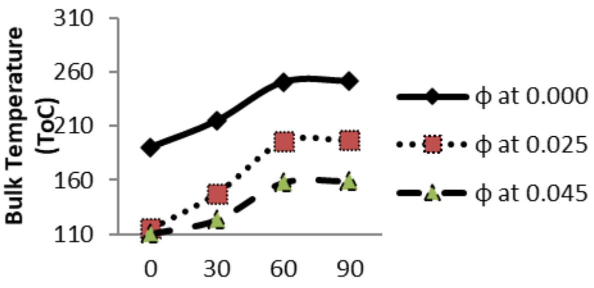

Figure 10. Distinction of bulk temperature with various angles of inclination at Gr = 10^6, Pr = 6.2, Re = 300, e = 0.866, Ha = 50, ω = 0, 0.025, 0.045

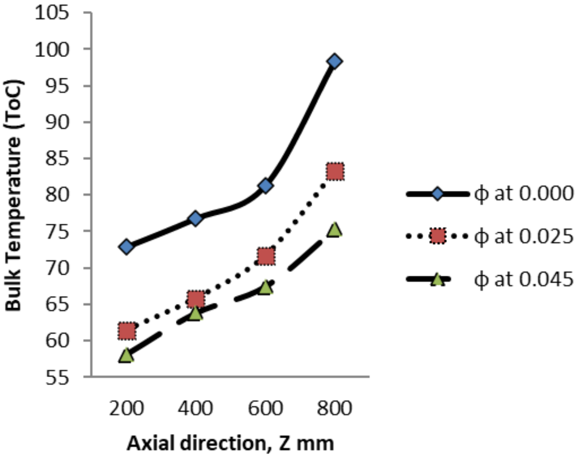

Figure 11. Distinction of the non-dimensional temperature profiles with different nanoparticle volume fraction of the center line in axial direction at θ = 30^0, Pr = 6.2, Re = 300, e = 0.866

3.3 Heat transfer characteristic (Nul and NUa) and enhancement

Figure 12 presents the consequence of eccentricity on the average Nusselt number. The rate of heat transfer elevated monotonically over the range $0 \leq e \leq 0.5$. The difference between the average Nusselt numbers was insignificant. Beyond this limit, $0.6 \leq e \leq 0.866$, the higher the value of eccentricity, e, the greater the rate of heat transfer. Again, within the range $0.6 \leq e \leq 0.866$, the rate of Nusselt number was no longer by convection only, conduction also occurred, a phenomenon that resulted in impulsive rise in the rate of heat transfer. Figure 13 shows the distinction of the average Nusselt number with different values of Reynolds number. For all Reynolds numbers considered, Re=1900 gave the utmost value of heat transfer, establishing that the higher the Reynolds number, the greater the rate of heat transfer. Figure 14 presents the outcome of inclination angles on the local Nusselt number. The plot gave a significant rate of heat transfer for the range $0^0 \leq \theta \leq 60^0$. Above this limit, that is, $60° \leq \theta \leq 90°$, there was no significant difference in the local Nusselt number because the gravitational force no longer had an effect on fluid flow. Figure 15 presents the conclusion regarding the Hartmann numbers on the average Nusselt number. The results indicated that, due to fluid flow within the elliptic configuration and the application of a magnetic field, the average heat transfer deteriorated with increasing Hartmann number (Ha).

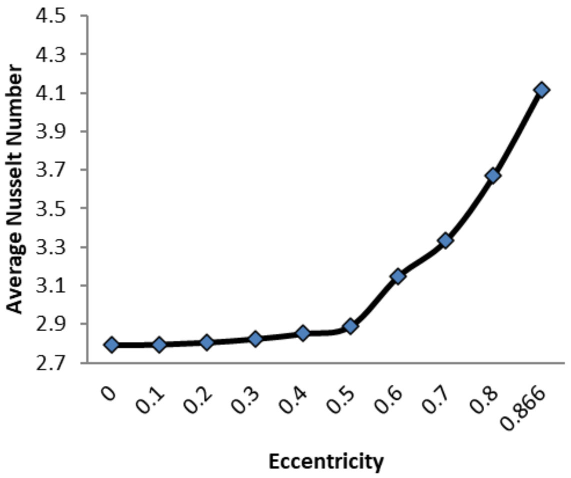

Figure 12. Distinction of average Nusselt number with different values of eccentricities at $\theta = 30^0$, Gr = 106, Pr = 6.2, Re = 300, Ha = 50, $\omega = 0.045$

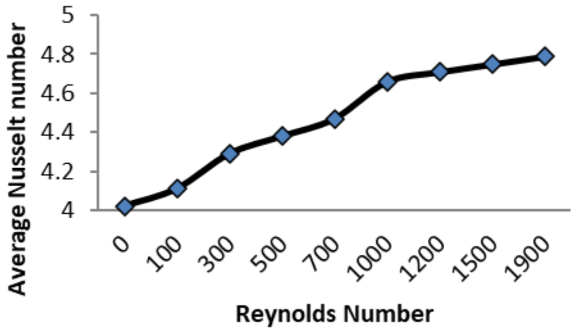

Figure 13. Variation of average rate of heat transfer with different values of Reynolds number at $\theta = 30^0$, Gr = 106, Ha = 50, Pr = 6.2, $\omega = 0.045$

Figure 16 shows the influence of varying Grashof number on the average Nusselt number. From the Figure, an elevating value of Grashof number ($Gr=10^6$) indicated a higher impact of secondary flow caused by natural convection effect. The rate of heat transfer enhancement of 193 % with $Gr=10^6$ was achieved when compared with the case of low Grashof number ($Gr=10^4$). Figure 17 presents the outcome of the average Nusselt number on different nanoparticle volume fractions. From the plot, augmenting nanoparticle volume fraction showed an increasing thermal conductivity of the nanofluid, immediate evidence of an enhanced thermal transport of the fluid flow in the elliptic enclosure, and consequently gave enhanced heat transfer of 14.39 % for solid volume fraction of $\omega = 0.045$ compared to the base fluid ($\omega = 0$).

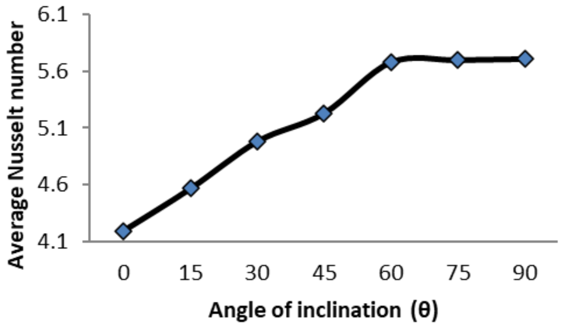

Figure 14. Distinction of local Nusselt number with angle of inclination at Gr = 106, Pr = 6.2, Ha = 50, Re = 300, $\omega = 0.045$

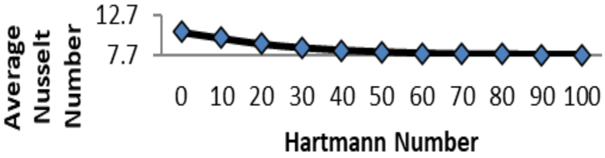

Figure 15. Distinction of Nusselt number with varying Hartmann number at $\theta = 30^0$, Gr = 106, Pr = 6.2, Re = 300, e = 0.866, $\omega = 0.045$

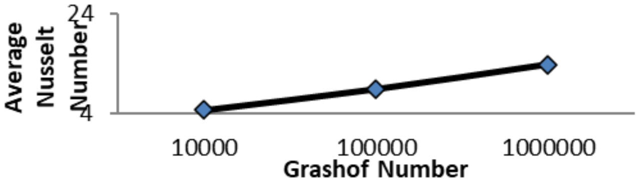

Figure 16. Deviation of average Nusselt number with varying Grashof number at $\theta = 30^0$, Pr = 6.2, Re = 300

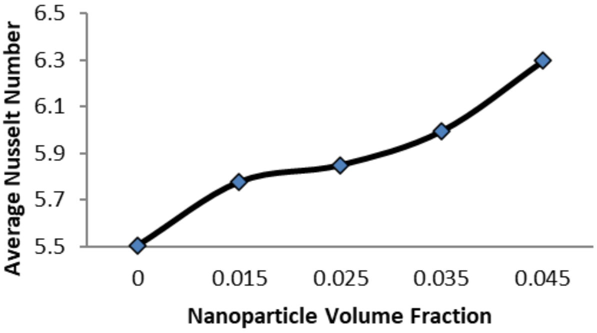

Figure 17. Effect of nanoparticle volume fractions (i.e ω = 0, 0.015, 0.025, 0.035, and 0.045) on average Nusselt number at θ = 300, Gr = 106, Pr = 6.2, Re = 300, e = 0.866

Figure 18 shows the disparity of convective heat transfer coefficient (h) with various nanoparticle volume fractions at the bottom heated wall along the axial direction. The Figure showed a distribution pattern that is symmetrical about the axial direction (Z=300 mm). It was established that the rate of heat transfer enhancement between the volume fraction of ω = 0.045 compared to the base fluid (ω = 0) was established to be about 5%. Figure 19 presents the consequence of the Richardson number on the average Nusselt number. From the plot, the average rate of heat transfer is elevated with increasing Richardson number (Ri). The reason for this behavior was a result of a very strong secondary flow caused by the free convection effect at a high Richardson number. 21.69% heat transfer enhancement was achieved for Ri = 10 when compared to Ri = 1.

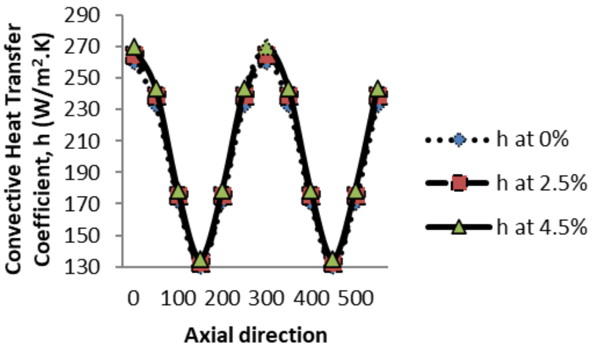

Figure 18. Distinction of convective heat transfer coefficient (h) with various nanoparticle volume fractions at the heated bottom wall along the axial direction at $\theta = 30^0$, Pr = 6.2, Re = 300, e = 0.866, Gr = 10^6.

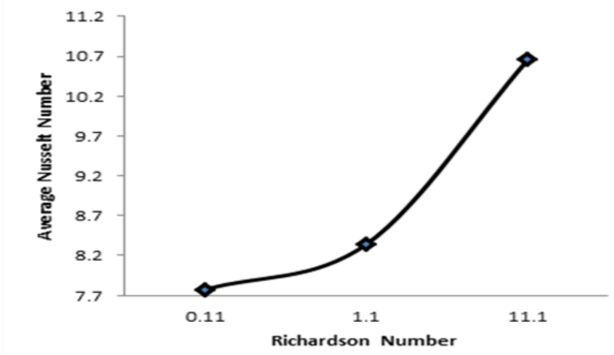

Figure 19. Disparity of Nusselt number with varying Richardson number (Ri) for $\theta = 30^0$, Gr = 10^4 - 10^6, Pr = 6.2, Re = 300, e = 0.866, ω = 0.045

4. Conclusion

A numerical study was carried out to analyze the heat transfer characteristics of Al_2O_3-H_2O nanofluid in an oriented elliptic configuration. The following conclusions were drawn from the study:

- The magnetic field effect (Ha) decreased with increasing fluid flow strength.
- Fluid flow motion was most significant within the range $0^0 \leq \theta \leq 30^0$, and the percentage increase was found to be 1.84 %. It was significant as well for the range $300 \leq \theta \leq 600$, but with a 0.5% increase. Above 60^0, that is, ($60^0 \leq \theta \leq 90°$), the impact of inclination became insignificant, owing to the gravitational force not having a noteworthy impact on the fluid flow again.
- The rate of heat transfer (Nu) augmented with increasing Grashof number, with an enhancement of 193 % for Gr at 106 when compared to Gr=10^4.
- Inclination angle enhanced the rate of heat transfer for $0° \leq \theta \leq 60°$ before becoming insignificant above this range ($60° \leq \theta \leq 90°$) as a result of less impact of gravitational force on the fluid flow.
- The variation of Reynolds number with Nusselt number was significant for 0≤Re≤1900
- The fluid circulation became pronounced, steady, and rigorous above a limit, that is, $0.7 \leq e \leq 0.866$, due to convection that became stronger than the heat transfer process
- The temperature decreased with increasing nanoparticle volume fractions (0.00 ,0.025 ,0.045).

Ethical issue

The authors are aware of and comply with best practices in publication ethics, specifically concerning authorship (avoidance of guest authorship), dual submission, manipulation of figures, competing interests, and compliance with policies on research ethics. The authors adhere to publication requirements that the submitted work is original and has not been published elsewhere in any language.

Data availability statement

The manuscript contains all the data. However, more data will be available upon request from the corresponding author.

Conflict of interest

The authors declare no potential conflict of interest.

References

[1] S.O. Oyedepo. Toward achieving energy for sustainable development in Nigeria. Renewable and Sustainable Energy Review, 34, (2014) ,255-273

[2] D. Ruchika, R. Puneet, and K. Lokendra . MHD mixed convection over an inclined cylinder subjected to velocity and thermal slip effect. Powder Technology, (2016). 288, 140 – 150.

[3] Al-Salem K., Ozto, H.R.,Pop,I, Varol, Y. (2012). Effects of moving lid direction on MHD convection in a linearly heated cavity. Int. Journal Heat and Mass Transfer, 55, 1103-1112.

[4] M. Fateh, and B. Rachid. Numerical modelling of MHD stability in a cylindrical configuration. Journal of the Franklin Institute, (2014) 351, 667-681.

[5] F.H. Ali, H.K. Hamzah and A. Abdulkadhim. Numerical study of mixed convection nanofluild in an annulus enclosure between outer rotating cylinder and inner corrugated cylinder.Heat transfer Asian res,(2019);48(1):343-360

[6] N. Morley, S.,Smolentser, and M. Abdan. MHD and Thermal issue on the SICF/SIC flow channel. Insent, Fusion Science and Technology, (2006) 50, 107-119

[7] S. Aberkane, M. Ihdere, M. Moderas, and A. Ghezal. Effect of an axial magnetic field on the heat and mass transfer in rotating annulus. Int. Journal. of Physical Science, (2014) 9, 368-379

[8] E.S. Ahmed, A. K., Hussein., H.A. Mohammad, I.K. Adegun, X. Zhang, L. Kolsi, A.Hasanpow, and S. Sivasankaran. Viscous dissipation and radiation effects on MHD natural convection in a square enclosure filled with a porous medium. Nuclear Engineering and Design, (2014), 266, 34-42

[9] M. Hasanuzzaman, F.O. Hakan, M. M., Raham, N.A. Rahim, R.,Saidur, and Y. Varol.

Magnetohydrodynamics natural convection in trapezoidal cavities. Int. Comm Heat Mass Transfer, (2012) 31,606-612.

[10] T. Hussein, A. Tuga, S. Kaz, A. ,Baoarudiw, A .A. ,Kadhim, and E. Sadeghinezhad. A review of studies on forced, natural and mixed heat transfer to fluid and nanofluid flow in an annular passage, Renewable and Sustainable Energy, (2014)39,835-856.

[11] S.K. Farid, M.M. Billah, M.M. Rahman, and U.Md.Sharif. MHD mixed convection in a lid-driven cavity having a heated circular hollow cylinder. Proceeding Engineering, (2013), 56, 474 – 479

[12] K.H. Wisam, and J. S. Gregory, J.S. Heat transfer in a high Hartmann number MHD duct flow with a circular cylinder around the heated wall. Int. J. of Heat and Mass Transfer, (2013) 67,944-954

[13] S. Fatih, and F.O. Hakan, Numerical study of MHD mixed convection in a nanofluid filled lid-driven square enclosure with a rotating cylinder. Int. J. of Heat and Mass Transfer, (2014). 78, 744-754

[14] M. S. Alam and M.A.H. Khan, M.A.H. (2014). MHD effects on mixed convection flow through a diverging channel with circular obstacles. 10th Int. Conference in Mechanical Engineering ICME 2013, Procedia Engineering, 90, 403-410.

[15] S. H. Muhammad, M. A. Alim, and H.K. Kazi.. Numerical analysis on MHD natural convection within trapezoidal cavity having circular block. American J. of Applied Mathematics and Statistics,(2016) 4(5),161-168

[16] E. Sourtiji, M. Gorji-Bandipy. D.D. Gangui, and S.M. Seyyedi. MHD buoyancy driven heat transfer in a cylindrical-triangular cavity filled with Cu-water nanofluid. Journal of Molecular Liquid, (2014), 196, 370 – 380

[17] B. Mahfoud, B. (2014). Swirling flow with heat transfer in a cylindrical under axial magnetic field. Recent Advances in Environmental Science and Biomedicine, 9, 45-50.

[18] B. R. Sharma, and H. Konwa,. MHD flow, heat and mass transfer about a horizontal cylinder in porous medium. Int. J. of Innovative Research in Science Engineering and Technology (IJIRSET), (2014) 3,1-10.

[19] W. Xiang, and S. M Arun. A review on nanofluids part II, experiments and applications. Brazilian Journal of Chemical Engineering, (2008) ,25 (4), 631-648

[20] U .S. Choi. Enhancing thermal conductivity of fluid with nanoparticles. Development and applications of non-newtonian flows. ASME, N/York, FED, (1995), 66, 99-105.

[22] T. Adekeye, I. K. Adegun, P. O. Okekunle, A.K. Hussein, S.O. Oyedepo, E. Adetiba, and O.S.I. Fayomi, Numerical analysis of the effects of selected geometrical parameters and fluid properties on MHD natural convection flow in an inclined elliptic porous enclosure with localized heating. Heat Transfer Asian Research, 46(3),(2017) 261-293.

[23] J.A. Chamkha, F. Salimefenchgil, and H.F. Oztop.. Effects of rotating cone on the mixed convection in a double lid-driven 3D porous trapezoidal nanofluid filled cavity, under the influence of magnetic field- nanomaterials,(2020) 10:1-17.

[24] T. Armaghani, H Esmaeli, Y.A. Mohammadpoor, I. Pop. MHD mixed convection flow and heat transfer in an open C-shaped enclosure using water-copper oxide nanofluid. Heat and mass transfer, (2018) 1-11

[25] N.Shukla, P. Rana, O. AnwarBeg, B. Singh, and A. Kadir, Homotopy study of MHD mixed convection nanofluid multiple slip flow as heat transfer over a vertical cylinder with entropy generation. Propulsion and power research, (2019), 8(2):147-162.

[26] A.J. Chamkha, A.M Rasheed, M.A, Ameghem, M.A. Mansour. Effect of partial slope on entropy generation and MHD combined convection in a lid-driven porous enclosure saturated with a Cu-water nanofluid of thermal. (2020), 132(2):1291-1306

[27] I K.,Adegun,. T.S. Jolayemi, O. A. Olayemi, and A.M Adebisi .Numerical simulation of forced convective heat transfer in inclined eliptic ducts with multiple internal longitudinal fins.Alexandra Engineering Journal,57,(2018) 2485-2496.

[28] R. B. Bird W. E. Stewart and E. N. Light foot. Transport phenomena 2nd edition, John Wiley, New York (2006). ISBN: 978-0-470-11539-8

[29] X. Wang, X. Xu, and S. U.S. Choi. Thermal conductivity of nanoparticles fluid mixture. Journal of Thermophysics and Heat Transfer,(1999) 13(4), 474-480.

[30] F. Selimefendigil and H. F. Oztop. MHD mixed convection of nanofluid filled partially heated triangular enclosure with a rotating adiabatic cylinder. Journal Taiwan Inst. Chem. Eng. In press.(2014) doi.org/10.1016/j.jtice

[31] M. Sheikholeslami, M, Gorji-Bandipy, D.D. Gangi. MHD influence in Al2O3-water based nanofluid in a concertic annulus Energy, (2013), 60, 501 – 510

[32] V.Javery,.Analysis of laminar thermal entrance region of elliptical and rectangular ducts with Kantorovish method, (1976) 85-98

[33] Sakalis,V.D., Hatzkonstaninoi,P.M.,Kafousias,N. (2002).Thermally developing flow in elliptic ducts with axially variable wall temperature distribution. International Journal of Meat and mass ransfer,45,25-35

[34] J. Amin. Numerical and experimental study of laminar forced convection heat transfer of TiO2-water nanofluid in triangular duct. Int. Journal of Artificial Intelligence and Mechatronics, (2014) 3(3), 107-111

[35] R.B. Mansour, N. Gelami, and C.T. Nguyen. Experimental investigation of mixed convection with water- Al2O3 nanofluid in inclined tube with uniform wall heat flux. Int. J. of Thermal Science, (2011), 50, 403 – 410.

Nomenclature

A	major radius of the enclosure, m
B	minor radius of the enclosure, m
b_0	magnetic field strength, tesla
c_p	specific heat capacity, J kg^{-1}K^{-1}
D_h	hydraulic diameter, m
e	dimensionless ellipse, eccentricity
T	dimensional temperature, K
G	acceleration due to gravity, m/s^2
Ha	Hartmann number
K	thermal conductivity, W m^{-1}K^{-1}
Gr	Grashof number
Nu_{av}	Average Nusselt number
Nu_l	Local Nusselt number
P	pressure, N/m^2
Pr	Prandtl number
Q	heat flux, w/m^2
R	dimensional radius, m
R	dimensionless radius, m
R	radial coordinate
Re	Reynolds number
Ri	Richardson number
T	dimensionless temperature, K
ΔT	dimensionless time step, s
U	dimensionless velocity component in radial direction
V	dimensionless velocity in the azimuthal direction
W	Dimensionless velocity component in axial direction
Z	Axial coordinate, m

Greek Symbols

α	thermal diffusivity , m^2/s
α_{nf}	thermal diffusivity of the nanofluid
$(\alpha)_{nf}$	thermal expansion of coefficient of nanofluid
β	thermal expansion coefficient, K^{-1}
θ	enclosure inclination angle, ^{0}C
ρ	fluid density , kgm^{-3}
σ_e	electrical conductivity, W/m^2
φ	Nanoparticle volume fraction
ρ_{nf}	effective density of nanofluid
$(\rho_{cp})_{n_j}$	specific heat of nanofluid
K_{nf}	thermal conductivity of nanofluid
μ_{nf}	dynamic viscosity of nanofluid
ϕ	azimuthal coordinate, m
υ	fluid kinematic viscosity, m^2/s

Abbreviations

b_f	Basefluid
F	Fluid
MHD	Magnetohydrodynamic
n_f	Nanofluid